RESEARCH ARTICLE
PLANETARY SCIENCE

Earth and Planetary Physics
2: 238–246, 2018
doi: 10.26464/epp2018023

Mapping of the lunar surface by average atomic number based on positron annihilation radiation from Chang'e-1

LiangQuan Ge[1], JianKun Zhao[2*], QingXian Zhang[1*], YaoYao Luo[1], and Yi Gu[1]

[1]College of Applied Nuclear Technology and Automation Engineering, Chengdu University of Technology, Chengdu 610059, China;

[2]School of Nuclear Science and Engineering, East China University of Technology, Nanchang 330013, China

Abstract: A map of the average atomic number of lunar rock and soil can be used to differentiate lithology and soil type on the lunar surface. This paper establishes a linear relationship between the average atomic number of lunar rock or soil and the flux of position annihilation radiation (0.512-MeV gamma-ray) from the lunar surface. The relationship is confirmed by Monte Carlo simulation with data from lunar rock or soil samples collected by Luna (Russia) and Apollo (USA) missions. A map of the average atomic number of the lunar rock and soil on the lunar surface has been derived from the Gamma-Ray Spectrometer data collected by Chang'e-1, an unmanned Chinese lunar-orbiting spacecraft. In the map, the higher average atomic numbers ($Z_A > 12.5$), which are related to different types of basalt, are in the maria region; the highest Z_A (13.2) readings are associated with Sinus Aestuum. The middle Z_A (~12.1) regions, in the shape of irregular oval rings, are in West Oceanus Procellarum and Mare Frigoris, which seems to be consistent with the distribution of potassium, rare earth elements, and phosphorus as a unique feature on the lunar surface. The lower average atomic numbers ($Z_A < 11.5$) are found to be correlated with the anorthosite on the far side of the Moon.

Keywords: average atomic number; Lunar rock and soil; positron annihilation radiation; Monte Carlo simulation; Chang'e-1 Gamma-ray spectrometer

Citation: Ge, L. Q., Zhao, J. K., Zhang, Q. X., Luo, Y. Y., and Gu, Y. (2018). Mapping of the lunar surface by average atomic number based on positron annihilation radiation from Chang'e-1. *Earth Planet. Phys.*, *2*(3), 238–246. http://doi.org/10.26464/epp2018023

1. Introduction

The average atomic number of lunar rock and soil is an important geophysical and geochemical parameter. A map of the average atomic number of lunar rock and soil can be used to differentiate lunar surface lithology and soil types. The relationship between fast neutron flux from the lunar surface and the average atomic mass of lunar soil was found by Gasnault (Gasnault et al., 2001), which confirmed that fast neutron leakage flux in the energy range of 0.6 to 8 MeV was proportional to average soil atomic mass. Accordingly, from the fast neutron spectra collected by the Lunar Prospector Fast Neutron Spectrometer (LPFNS), a map of the average atomic mass of lunar rock and soil was obtained with a precision of ~20%.

The Gamma-Ray Spectrometer (GRS) aboard the Chinese lunar-orbiting spacecraft Chang'e-1 provides the distribution of major elements O, Si, Mg, Al, Ca, Na, and Fe (Hasebe et al., 2009; Kobayashi et al., 2012) and natural radioactive elements U, Th, and K on the lunar surface (Hasebe et al., 2009; Ouyang ZY et al., 2011; Zhu MH et al., 2013, 2015). During the Chang'e-1 mission, the spacecraft stayed in a circular polar orbit with a period of 127 minutes at a nominal altitude of 200 km. Global GRS data over intervals of 3 seconds were obtained from the in-flight gamma spectra in the energy range of 0.1 to 9 MeV (Hasebe et al., 2009; Ma T et al., 2008; Yang J et al., 2013; Zhu MH et al., 2010).

The high-energy gamma rays from the lunar surface originate predominantly from cosmic neutron and proton interactions with lunar rocks and soil (Reedy, 1978). Some characteristic gamma rays are identified from GRS data (Hasebe et al., 2009; Yang J et al., 2013; Zhu MH et al., 2010). GRS peaks at or near 0.512, 0.58–0.61, 1.46, 1.80, 2.20–2.62, 6.1, 6.76, and 7.1–7.6 MeV are associated with position annihilation radiation (PAR) and natural or induced radiation from the elements U, Th, K, Al, Si, O, Ti, and Fe (Yang J et al., 2013; Zhu MH et al., 2011).

This paper investigates the relationship between 0.512-MeV PAR intensities and the average atomic number of lunar rock and soil. First, an analytical model suggests a linear relationship between the PAR flux from the lunar surface and the average atomic mass of surface rock and soil. Second, the analytical model is found to agree well with results of the Monte Carlo simulation. Finally, a map of the average atomic number, obtained by the model with data from the Chang'e-1 GRS, is constructed.

2. Theory

The 0.512-MeV gamma rays are generated from PAR, in which the positron is from pair production (Knoll, 2000). In Figure 1, we consider a simplified physical model for calculating the flux of 0.512-

Correspondence to: J. K. Zhao, martin1945@ecit.cn
Q. X. Zhang, shinecore@163.com
Received 27 OCT 2017; Accepted 25 APR 2018.
Accepted article online 09 MAY 2018.

MeV gamma rays emitted from the lunar surface as a semi-infinite homogeneous medium. In the model it is assumed that the yield of gamma rays induced by the cosmic rays is a constant over the depth of interest.

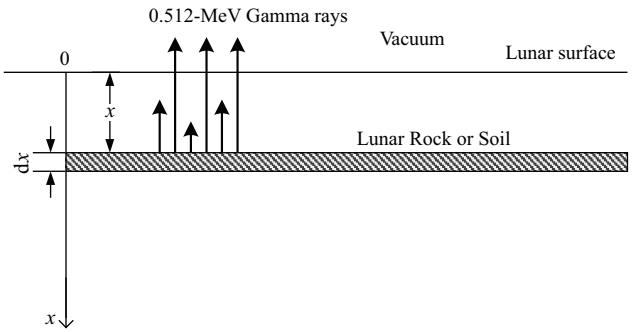

Figure 1. Diagrammatic sketch of the leakage of 0.512-MeV photons from the lunar surface.

The flux of annihilation photons produced in a thin layer of thickness dx is given by

$$\mathrm{d}I_{\mathrm{d}x} = \sum_{j=1}^{m} \frac{2\rho C_j N_{\mathrm{A}} \mathrm{d}x}{A_j} \sum_{i=1}^{n} K_{ij} I_{E_i}, \tag{1}$$

where A_j is the atomic mass of the jth element in layer dx, C_j is the mass fraction of the jth element in layer dx in percent, ρ is the density of lunar soil or rock in grams per cubic centimeter, I_{E_i} is the flux of excitation gamma rays in the layer with energy E_i, in cm^{-2} s^{-1}, N_{A} is the Avogadro's constant, 6.02×10^{23}, the coefficient of 2 indicates that two annihilation photons are generated per pair-production interaction, and K_{ij} is the probability of pair-production interaction between a photon of energy E_i and an atom of element Z_j, which can be given by (Knoll, 2000)

$$K_{ij} = kZ_j^2 \ln E_i, \tag{2}$$

where k is a constant, and E_i, in MeV, is the ith energy above 1.02 MeV.

Equation (1) can be rewritten as

$$\mathrm{d}I_{\mathrm{d}x} = 2\rho k N_{\mathrm{A}} \mathrm{d}x \sum_{j=1}^{m} \frac{C_j Z_j^2}{A_j} \sum_{i=1}^{n} I_{E_i} \ln E_i. \tag{3}$$

Because the lunar rock and soil mainly consists of petrogenetic elements, the ratio of Z_j to A_j approximates to 0.5. Therefore, Equation (3) transforms to

$$\mathrm{d}I_{\mathrm{d}x} = \rho k N_{\mathrm{A}} \mathrm{d}x \sum_{j=1}^{m} C_j Z_j \sum_{i=1}^{n} I_{E_i} \ln E_i. \tag{4}$$

The flux of 0.512-MeV gamma rays emitted from layer dx will attenuate through upper layers to the lunar surface (see Figure 1). The flux of 0.512-MeV gamma rays from layer dx to the lunar surface can be given by

$$\mathrm{d}I_{0.512} = \mathrm{d}I_{\mathrm{d}x} \mathrm{e}^{-\mu_{0.512} x}, \tag{5}$$

where $\mu_{0.512}$ is the linear attenuation coefficient of 0.512-MeV gamma rays for the lunar medium in cm^{-1}.

The flux of 0.512-MeV gamma rays leaking out the lunar surface, $I_{0.512}$, is an integral over the semi-infinite layer.

$$\begin{aligned} I_{0.512} &= \int_0^{\infty} \mathrm{d}I_x \mathrm{e}^{-\mu_{0.512} x} \mathrm{d}x \\ &= \rho k N_{\mathrm{A}} \sum_{j=1}^{m} C_j Z_j \sum_{i=1}^{n} \mu_{E_i} I_{E_i} \ln E_i \int_0^{\infty} \mathrm{e}^{-\mu_{0.512} x} \mathrm{d}x \\ &= \frac{\rho k N_{\mathrm{A}}}{\mu_{0.512}} Z_{\mathrm{A}} \sum_{i=1}^{n} \mu_{E_i} I_{E_i} \ln E_i, \end{aligned} \tag{6}$$

where $Z_{\mathrm{A}} = \sum_{j=1}^{m} C_j Z_j$ is the average atomic number of the rock and soil on the lunar surface.

The flux of gamma rays with energy E_i induced by cosmic rays striking the lunar surface, $I_{E_i}^{\mathrm{o}}$, is given as following

$$\begin{aligned} I_{E_i}^{\mathrm{o}} &= \int_0^{\infty} I_{E_i} \mathrm{e}^{-\mu_{E_i} x} \mathrm{d}x \\ &= \frac{I_{E_i}}{\mu_{E_i}}, \end{aligned} \tag{7}$$

where I_{E_i} is the yield of gamma rays in the thin layer and is assumed as a constant, μ_{E_i} is the linear attenuation coefficient of the lunar rock and soil for gamma rays with energy E_i, in in cm^{-1}. μ_{E_i} can be calculated by XCOM software, which is developed by the National Institute of Standards and Technology.

From Equation (6), the average atomic number of the lunar rock and soil can be expressed as a function of $I_{E_i}^{\mathrm{o}}$ and $I_{0.512}$,

$$Z_{\mathrm{A}} = a \cdot \frac{I_{0.512}}{\sum_{i=1}^{n} \mu_{E_i} I_{E_i}^{\mathrm{o}} \ln E_i}, \tag{8}$$

where $a = \frac{\mu_{0.512}}{\rho k N_{\mathrm{A}}}$ is a coefficient that could be obtained by Monte Carlo simulation, as described in Section 3. The net peak area, N_{E_i}, is as

$$N_{E_i} = \varepsilon_i I_{E_i}, \tag{9}$$

where ε_i is the peak efficiency of the gamma-ray spectrometer at energy E_i.

From Equations (8) and (9), we get

$$Z_{\mathrm{A}} = a \frac{N_{0.512}/\varepsilon_{0.512}}{\sum_{i=1}^{n} \mu_{E_i} \ln E_i \cdot N_{E_i}^{\mathrm{o}}/\varepsilon_{E_i}}, \tag{10}$$

where $N_{0.512}$ and $N_{E_i}^0$ are the net peak areas with 0.512-MeV and E_i. In this equation the net peak areas are obtained from Chang'e-1 GRS data, and the peak efficiency of $\varepsilon_{0.512}$ and ε_i can be obtained by Monte Carlo simulations.

3. Monte Carlo Simulation

3.1 Simulation of the PAR Flux Emitted from the Lunar Surface

The Geant4 Monte Carlo code has been used to simulate the

gamma ray spectra from the lunar surface (Gurtner et al., 2006; Ohishi et al., 2004; Yamashita et al., 2008). The model consists of a cylinder which is filled with the lunar rock and soil with a density of 2.0 g/cm^3 and a 40cm-diameter sphere current detector, as shown in Figure 2. The detector is placed on the axis of the cylinder, 0.5 m above the cylinder's upper surface. Six types of lunar rock, including KREEP, anorthosite, dunite, high alumina basalt, low titanium basalt, and high titanium basalt, are used to study the relationship between the average atomic number and the flux of 0.512-MeV gamma rays. The compositions and average atomic numbers of the six lunar rocks are given in Table 1 (Heiken et al., 1991).

Table 1. Compositions and average atomic numbers of six lunar rocks

Sample ID lithology	#12038 High alumina basalt	#15405 KREEP	#14053 Anorthosite	#72417 Dunite	#12002 Low titanium basalt	#10003 High titanium basalt
			Compositions (wt%)			
O	41.62	44.04	46.13	43.10	40.70	38.32
Na	0.50	0.67	0.22	0.01	0.17	0.30
Mg	4.05	2.17	0.15	27.24	8.90	4.04
Al	6.73	6.74	18.63	0.69	4.15	5.54
Si	21.92	26.58	20.84	18.56	20.26	18.70
K	0.06	1.73	0.02	0.02	0.04	0.05
Ca	8.27	5.84	13.75	0.77	5.87	7.98
Ti	2.81	1.62	0.01	0.03	2.24	9.16
Cr	0.05	<0.01	<0.01	0.23	0.65	0.17
Mn	0.20	<0.01	0.01	0.09	0.22	0.23
Fe	13.79	10.61	0.24	9.26	16.80	15.51
Average Atomic Number	13.75	13.07	11.89	12.06	13.97	14.67

The primary source beam injected into the lunar rock and soil is 100-MeV protons. The energy range of gamma ray spectra is from 0.01 to 10 MeV and the energy interval is 4.89 keV. The number of history events is set as 2.0×10^9 and the statistical error of results is <5% in any energy bin.

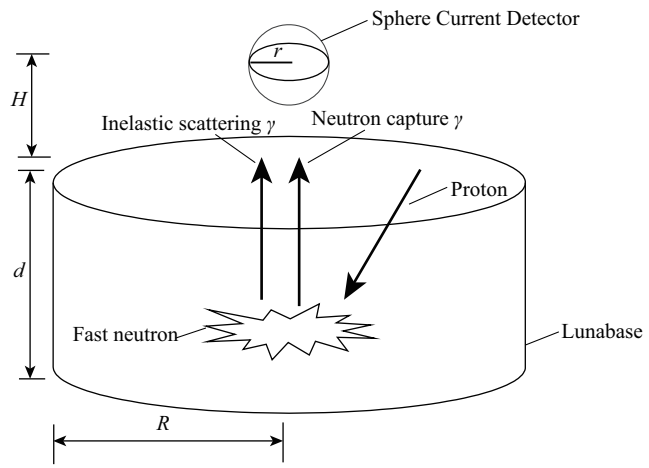

Figure 2. Geant4 simulation model of proton-induced gamma rays.

Figure 3 shows the gamma-ray spectrum simulated by Geant4 Monte Carlo code of low titanium basalt. The spectrum is composed of characteristic gamma lines with discrete energies and scattered gamma rays with continuous energies. The 0.512-MeV gamma line has the highest flux. Higher flux of gamma lines are found at 0.847 MeV (^{56}Fe), 1.37 MeV (^{24}Mg), 1.78 MeV (^{28}Si), and 6.13 MeV (^{16}O). These are the major elements of the low titanium basalt. Some other lines from ^{16}O (7.12, 6.91, 4.44, and 3.68 MeV), ^{27}Al (3.00, 2.21, and 1.01 MeV), ^{28}Si (2.84 MeV), and ^{40}Ca (3.74 MeV), produced from neutron inelastic scattering, can be acquired. In addition, a fraction of the gamma rays in the spectrum are produced by neutron capture (e.g., 4.93 MeV (^{28}Si), 6.76 MeV (^{48}Ti), and 7.64 MeV (^{56}Fe)) (Reedy, 1978, 2000, 2013). The simulation results for the PAR flux and higher flux gamma lines for the six lunar rocks are given by Table 2.

The flux of PAR and induced gamma rays in the six lunar rocks, calculated by Geant4 Monte Carlo code, are listed in Table 2. The $\sum_i^n \mu_{E_i} I_{E_i}^0 \ln E_i$ is calculated in table, which the average value μ_{E_i} used is list in Table 3.

3.2 Simulation of the Linear Attenuation Coefficients and Constant *a*

The μ_{E_i} of KREEP, anorthosite, dunite, high alumina basalt, low titanium basalt, and high titanium basalt are listed in Table 3. The relative errors of μ_{E_i} between the average value and each lithology are <±2%.

The relationship between the ratio of $I_{0.512}$ to $\sum_{i=1}^n \mu_{E_i} I_{E_i}^0 \ln E_i$ and Z_A is shown in Figure 4. The *a* in Equation (10) for calculating the average atomic number of the lunar rock and soil is obtained by linear fitting. The *a* values for the six lunar rocks are listed in Table 2 and the average *a* for lunar rocks and soils is 1.10.

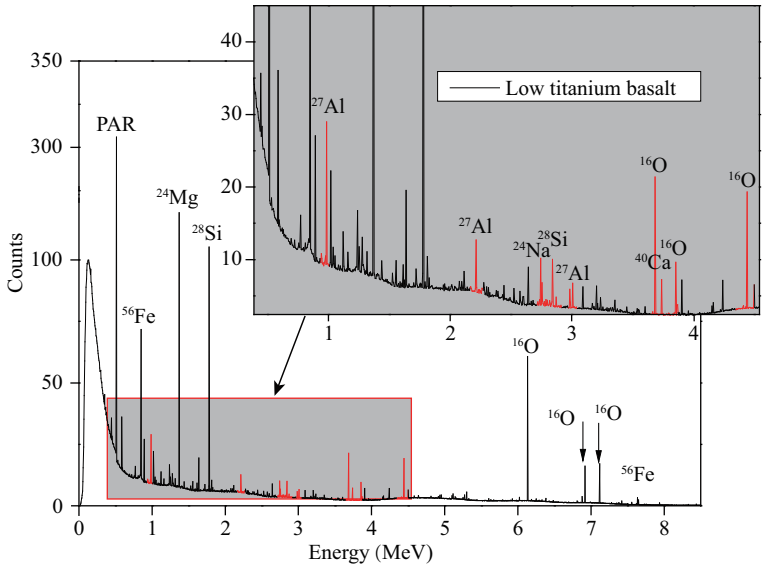

Figure 3. The spectrum by Geant4 Monte Carlo code of low titanium basalt. The characteristic peaks between 1 and 4.5 MeV are marked in red.

Table 2. Gamma flux from six lunar rocks simulated by Geant4 Monte Carlo code*

Nuclide	Energy (MeV)	Reaction mode	High alumina basalt	KREEP	Anorthosite	Dunite	Low titanium basalt	High titanium basalt
			I_{E_i} (cm^{-2})					
–	0.512	PAR	297.97(1.8)	288.48(1.8)	257.98(1.2)	323.01(1.4)	305.93(1.3)	316.65(1.3)
	7.12		1.20(3.7)	1.16(3.5)	1.16(3.5)	1.27(3.7)	1.23(3.7)	1.18(3.7)
^{16}O	6.91		16.57 (14.2)	17.42(14.1)	17.66(13.3)	16.62(14.4)	16.17(14.0)	15.79(13.8)
	6.13		62.27(2.0)	65.18(1.9)	66.99(1.9)	61.23(2.0)	60.75(2.0)	59.38(2.1)
	4.44		19.12(3.6)	19.71(3.5)	19.56(3.5)	21.67(3.4)	19.31(3.6)	18.50(3.6)
	3.68		21.84(12.3)	22.59(12.0)	23.12(12.7)	21.25(12.3)	21.37(12.2)	21.32(11.3)
^{24}Mg	1.37		58.16(2.0)	33.90(6.7)	8.14(6.3)	320.76(0.9)	119.16(4.8)	60.57(2.1)
^{27}Al	3.00		8.87(5.4)	8.65(7.1)	17.75(3.6)	3.51(9.7)	6.73(6.5)	8.31(6.3)
	2.21	(n, nγ)	17.13(3.9)	16.66(4.7)	34.80(2.5)	6.18(7.5)	12.70(4.6)	15.88(4.1)
^{28}Si	2.84		10.61(5.0)	11.94(4.9)	9.82(5.0)	8.54(5.6)	10.02(5.1)	10.25(5.1)
	1.78		112.97(1.4)	132.86(1.4)	99.99(1.5)	85.48(1.6)	105.22(1.5)	102.67(1.5)
^{40}Ca	3.74		9.09(5.3)	6.93(5.8)	12.19(4.4)	3.07(10.3)	7.25(6.1)	10.28(5.0)
^{28}Si	4.93		4.40(8.0)	4.84(7.9)	4.90(7.1)	5.33(7.0)	4.41(7.9)	4.09(8.4)
^{48}Ti	6.76	(n, γ)	1.40(14.8)	1.43(15.3)	1.36(15.3)	1.55(14.2)	1.45(14.9)	1.44(14.7)
^{56}Fe	7.64		2.78(7.3)	2.52(6.4)	0.64 (20.5)	4.37(5.5)	3.46(6.3)	2.35(8.2)
	$\sum_i^n \mu_{E_i} I^{\circ}_{E_i} \ln E_i$		23.88(30.0)	24.51(30.2)	24.12(33.5)	29.78(27.9)	24.72(29.1)	22.82(32.3)
	$\frac{I_{0.512}}{\sum_i^n \mu_{E_i} I^{\circ}_{E_i} \ln E_i}$		12.48(30.1)	11.77(30.3)	10.70(33.5)	10.85(27.9)	12.38(29.1)	13.88(32.3)
	a		1.10(30.1)	1.11(30.3)	1.11(33.5)	1.11(27.9)	1.13(29.1)	1.06 (32.3)

Notes: *The values in parentheses present the relative errors for $I^{\circ}_{E_i}$ in unit of millesimals, provided by the Geant4 Monte Carlo code, and the others are the transfer relative errors. In particular, the relative errors for the average atomic number "Z_A" cannot be acquired. Consequently, the transfer relative errors for "a" are instead that of $I_{0.512}/\sum_{i=1}^{n} \mu_{E_i} I^{\circ}_{E_i} \ln E_i$.

Table 3. The μ_{E_i} of KREEP, anorthosite, dunite, high alumina basalt, low titanium basalt, and high titanium basalt

Energy (MeV)	#12038 High alumina basalt	#15405 KREEP	#14053 Anorthosite	#72417 Dunite	#12002 Low titanium basalt	#10003 High titanium basalt	Average value
	Linear attenuation coefficient μ_{E_i}($\times10^{-2}$ cm^{-1})						
1.37	17.14	17.17	17.21	17.18	17.12	17.07	17.15
1.78	10.72	10.75	10.80	10.77	10.71	10.66	10.73
2.21	9.38	9.41	9.44	9.42	9.37	9.34	9.39
2.84	8.41	8.42	8.45	8.42	8.40	8.38	8.41
3.00	7.44	7.45	7.45	7.43	7.44	7.43	7.44
3.68	7.25	7.25	7.26	7.24	7.25	7.24	7.25
3.74	6.61	6.60	6.59	6.57	6.61	6.61	6.60
4.44	6.57	6.56	6.54	6.52	6.56	6.57	6.55
4.93	6.11	6.09	6.06	6.05	6.11	6.12	6.09
6.13	5.86	5.84	5.80	5.79	5.87	5.89	5.84
6.76	5.43	5.40	5.34	5.33	5.44	5.47	5.40
6.91	5.27	5.23	5.16	5.15	5.28	5.32	5.24
7.12	5.24	5.19	5.12	5.11	5.25	5.29	5.20
7.64	5.19	5.15	5.07	5.07	5.21	5.25	5.16

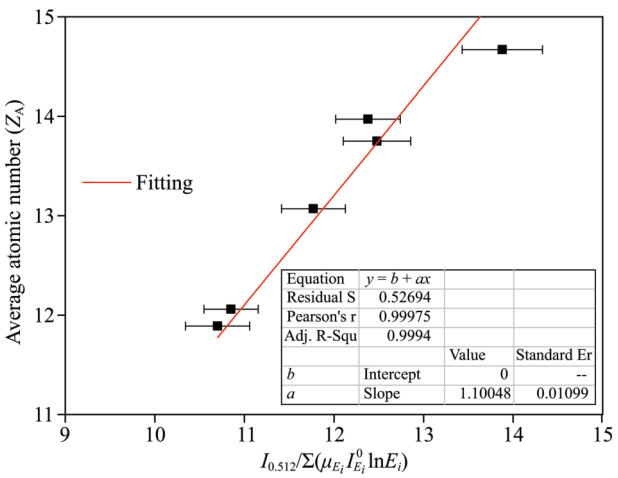

Figure 4. Relationship between average atomic number and $\dfrac{I_{0.512}}{\sum_{i=1}^{n} \mu_{E_i} I^0_{E_i} \ln E_i}$.

3.3 Simulation of Peak Efficiency of the GRS

To calculate the average atomic number of the lunar rock and soil from Chang'e-1 GRS data, the peak efficiency ε_i of the Chang'e-1 GRS is determined at 0.512 MeV and other high energies by Geant4 Monte Carlo code simulation. The gamma-ray source used in simulation uniformly distributes on a surface. The relative peak efficiency to that at 0.512 MeV, are given in Table 4.

Table 4. Relative gamma peak efficiencies calculated by Geant4 Monte Carlo code simulation

Energy (element) (MeV)	Relative peak efficiency $\varepsilon_i/\varepsilon_{0.512}$ (%)
0.512	100
1.12(^{214}Bi)	56.51(0.87)*
1.37 (^{24}Mg)	48.98(0.51)
1.46 (^{40}K)	47.34(0.73)
1.76(^{214}Bi)	44.57(0.74)
1.78 (^{28}Si)	44.23(0.23)
2.21(^{27}Al)	41.07(0.49)
2.62(^{208}Tl)	39.44(0.99)
2.84 (^{28}Si)	39.33(0.54)
3.00(^{27}Al)	39.17(0.67)
3.74(^{40}Ca)	38.88(0.64)
4.93 (^{28}Si)	38.76(0.81)
6.76 (^{48}Ti)	38.24(1.50)
7.64 (^{56}Fe)	38.11(0.66)

Notes: *Values in parentheses present the relative transfer errors for $\varepsilon_i/\varepsilon_{0.512}$.

4. Average Atomic Number of Rock and Soil on Lunar Surface

4.1 Gamma-ray Spectra from Chang'e-1

2467169 spectra recorded by Chang'e-1 GRS (Ma T et al., 2008) are used to map the average atomic number of rock and soil on lunar surface. A map with grid of 150 km×150 km is applied to cover the Moon.

The spectrum, as shown in Figure 5, is the sum of all the available spectra in different flight cycles of Chang'e-1 GRS in the same grid. The background, estimated by a fast-Fourier-transform numerical

method (Zhang QX et al., 2012), and net spectrum are also shown in Figure 5. As seen in the figure, the 0.512 MeV peak from the PAR is obvious. Other peaks corresponding to isotopes in the lunar rock and soil also can be easily identified: e.g., at 0.6 MeV (^{214}Bi+^{208}Tl), 1.45 MeV (^{24}Mg+^{40}K), 1.78 MeV (^{28}Si+^{214}Bi), 2.1–2.7 MeV (^{27}Al+^{208}Tl), 5.8–6.7 MeV (^{16}O+^{48}Ti), and 7.64 MeV (^{56}Fe). A subset of these peaks, at 1.45 MeV (^{24}Mg+^{40}K), 1.78 MeV (^{28}Si+^{214}Bi), 2.1–2.7 MeV (^{27}Al+^{208}Tl), 6.76 MeV (^{48}Ti), and 7.64 MeV (^{56}Fe), are selected for evaluating the average atomic numbers by Equation (10). The energy ranges of these peaks are defined in

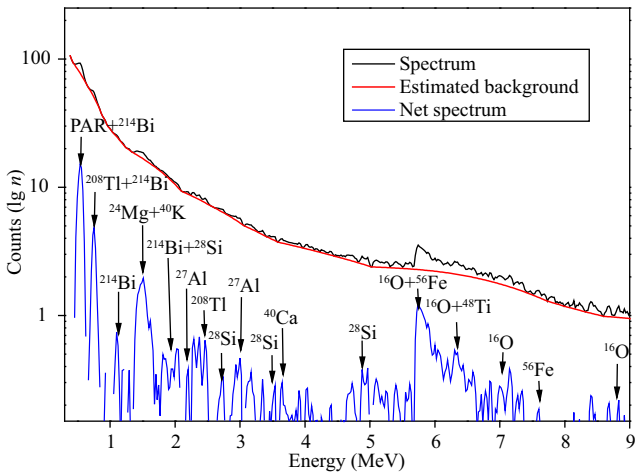

Figure 5. Gamma-ray spectrum recorded by Chang'e-1 GRS in the region of Mare Imbrium.

Table 5. Energy range of peaks in spectrum recorded by Chang'e-1 GRS

Energy(element) (MeV)	Energy band (MeV)
0.512	0.466 to 0.558
1.12(^{214}Bi)	1.03 to 1.23
1.45 (^{40}K+^{24}Mg)	1.26 to 1.63
1.78 (^{214}Bi+^{28}Si)	1.65 to 1.91
2.21(^{27}Al)	1.96 to 2.38
2.62(^{208}Tl)	2.42 to 2.70
2.84 (^{28}Si)	2.72 to 2.90
3.00(^{27}Al)	2.89 to 3.11
3.74(^{40}Ca)	3.60 to 3.87
4.93 (^{28}Si)	4.75 to 5.11
6.76 (^{48}Ti)	4.66 to 7.00
7.64 (^{56}Fe)	7.36 to 7.91

Table 5. $\varepsilon_i/\varepsilon_{0.512}$, a and μ_{E_i} are obtained in section 3.

The peak at ~6.0 MeV, from the inelastic scattering of fast neutrons on oxygen, is not used to evaluate the average atomic number of lunar rock and soil, because the fuel tank is near the GRS and the residual oxygen cannot be quantified during the Chang'e-1 mission.

To acquire the net counts directly from PAR at 0.512 MeV, the overlapping portion from the 0.511-MeV gamma rays of ^{208}Tl should be removed since the relative emission fraction of the 0.511-MeV gamma ray from ^{208}Tl is 25% of its 2.62-MeV gamma ray. The relative efficiency to ^{208}Tl is 39.44% (to PAR). So when calculating the net peak area of the 0.511-MeV, the contribution from ^{208}Tl, amounting to 63.38% of the area of the 2.62-MeV gamma ray, should be removed.

4.2 Map of Average Atomic Number of the Lunar Surface

To verify the results of Figure 6, average atomic numbers of the lunar rock and soil at points where Apollo and Luna rovers landed and took samples are recorded. The scatter diagram of the atomic mass of samples from the A11, A12, A15, A16, A17, L16, L20, and L24 mission (Gasnault et al., 2001) and the average atomic numbers are plotted in Figure 7. The error bars on average atomic number are the transferred relative errors of "a", "μ_{E_i}" and the GRS measurement statistical errors. As seen in Figure 7, the correlation coefficient is 0.7176 between average atomic number and average atomic mass.

As seen in Figure 6, the higher Z_A value region corresponds to lunar maria, such as Mare Frigoris (56.0°N, 1.4°E), Mare Vaporum (13.3°N, 3.6°E), Mare Australe (38.9°S, 93.0°E), and Mare Imbrium (32.8°N, 15.6°W) (Jolliff et al., 2000). This result is in agreement with the results of average atomic mass mapping by the Lunar Prospector Neutron System (LP-NS) (Elphic et al., 1998; Feldman et al., 1998; Gasnault et al., 2001), especially on the edge of Mare Vaporum and Mare Insularum (7.5°N, 30°W), close to Sinus Aestuum (10.9°N, 8.8°W), with a Z_A value up to 13.2. Its regional strike tends southwest throughout the Mare Imbrium and Mare Vaporum, corresponding to the Apollo gamma-ray system data: A majority of maria are covered by different types of basalt, all of which have a higher average atomic number than other lunabase (Hasebe et al., 2009; Haskin, 1998; Zhu MH et al., 2010). In addition, some craters, such as Schwarzshild (70.1°N, 121.2°E), have a higher Z_A value. As a consequence of meteorite collision impact, dark basalt, including some heavier elements, is deposited in the bottoms of craters. Therefore, these regions display a notable characteristic in the map of average atomic number.

A couple of medium Z_A value (~12.5) regions can be identified on the Z_A map. Two of them, surrounded by irregular oval rings, are West Oceanus Procellarum and Mare Frigoris. Others are around some large craters, such as Sinus Iridum (44.1°N, 31.5°W). These regions seem to be consistent with the distribution of KREEP as a unique feature on the lunar surface. Although the reason for the unique shape of average atomic number areas is still an open issue, petrogenesis, impact melting (Delano and Ringwood, 1978), or magma upwelling (Dymek, 1986; McKay, 1986; Taylor, 1982) are considered possibilities. Diagenesis certainly played a significant role in compositional differentiation. Therefore, the regionalized medium Z_A value concentration is affected by the course of magmatism beneath the KREEP terrane (Taylor, 2014; Taylor et al., 2006).

Other than the above high and medium Z_A regions, the majority of the lunar surface has lower average atomic numbers. This is because the region is widely covered with lunabase, which basically

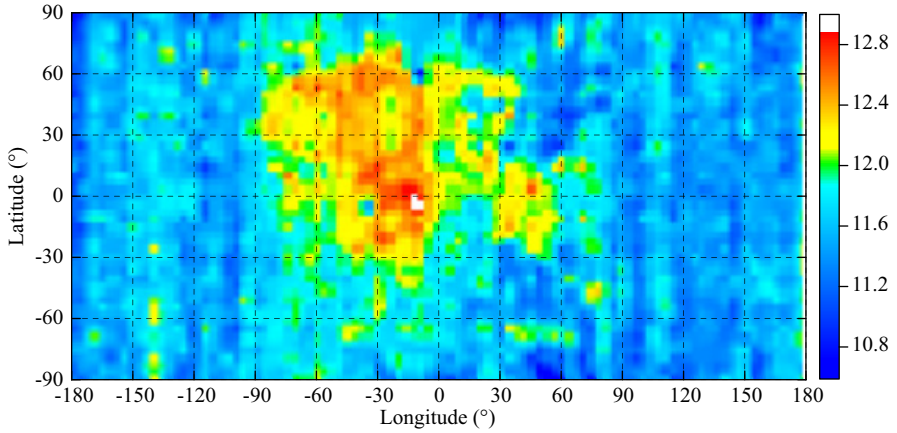

Figure 6. The map of average atomic numbers of rock and soil on the lunar surface (with coordinate values for south and west being negative).

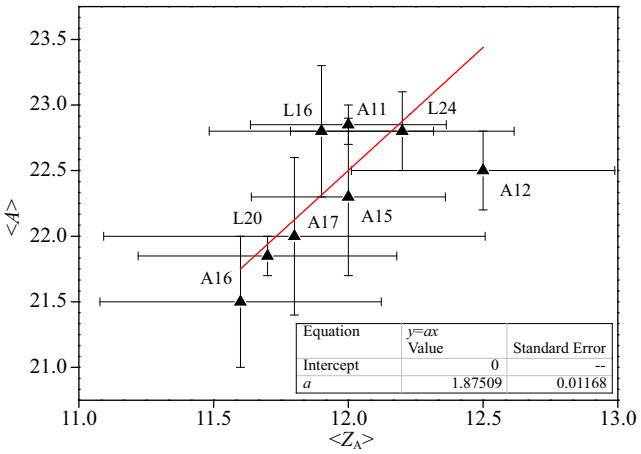

Figure 7. The scatter diagram of the atomic mass of lunar rocks and soils samples from A11, A12, A15, A16, A17, L16, L20, and L24 missions and the average atomic number.

consists of mafic anorthosite (Korotev et al., 2003) and bytownite anorthosite (Norman and Ryder, 1980; Warren, 1993, 2005), both of which are rich in light elements, such as Mg, Ca, Na, and Ti.

From the above discussion, a couple of significant points can be summarized. First, there is a strong correlation between the average atomic number and the concentration of iron in maria regions, which is confirmed by gamma-ray spectra (Feldman et al., 2002; Lawrence et al., 2002), neutron spectra (Elphic et al., 2002, 1998, 2000), and multispectral analysis (Ling ZC et al., 2011; Yan BX et al., 2012). Second, there some high Z_A value spots surrounding the maria and scattered throughout the Moon. In the terrane, these spots typically appear in crater areas. Lunar craters are a result of meteorite impact. Their structure allows the mantle below the impact basin to upwell into the crater bottom and deposit basalt (with a high Z_A value) that easily permeates into the lithosphere (Phillips and Lambeck, 1980; Wise and Yates, 1970). This phenomenon is referred to as a mascon in geodetic gravimetry (Byrne et al., 2015; Freed et al., 2014; Melosh et al., 2013; Miljković et al., 2015; Montesi, 2013; Thorey et al., 2015). Third, the average atomic number in sinus areas is found on the gradient features (from 12 to 13). As an extended part from the highlands to maria, sinus have both characteristics. Therefore, in Figure 6 some sinus are filled with gradient color, such as Sinus Aestuum and Sinus Iridum.

5. Conclusions

A linear approximation for the relationship between position annihilation radiation gamma flux from the lunar surface and the average atomic number of lunar rocks or soil has been established. A simplified Monte Carlo model has been developed to confirm this method for evaluating average atomic number of the rock and soil on the lunar surface. The method has been used to construct a map of average atomic number on a 150 km×150 km grid from the Chang'e-1 GRS. The global map of average atomic number can differentiate the various types of lithology. The higher average atomic number (Z_A>12.5) located in the maria regions is closely related to different types of basalt, with the highest Z_A value of 13.2 found near Sinus Aestuum (10.9°N, 8.8°W). The West Oceanus Procellarum and Mare Frigoris regions surrounded by irregular oval rings are found to have medium Z_A values (~12.1), which seems to be consistent with the distribution of KREEP as a unique feature on the lunar surface. The lower average atomic number (Z_A<11.5) regions cover the majority of the lunar surface that is relatively dominated by anorthosite.

Acknowledgments

This research was supported by the National High-tech R&D Program (No. 2017YFC0602100) and the Natural Science Foundation of China (No. 41374136).

References

Byrne, P. K., Klimczak, C., McGovern, P. J., Mazarico, E., James, P. B., Neumann, G. A., Zuber, M. T., and Solomon, S. C. (2015). Deep-seated thrust faults bound the Mare Crisium lunar mascon. *Earth Planet. Sci. Lett.*, *427*, 183–190. https://doi.org/10.1016/j.epsl.2015.06.022

Delano, J. W., and Ringwood, A. E. (1978). Siderophile elements in the lunar highlands-nature of the indigenous component and implications for the origin of the Moon. In *Proceedings of the 9th Lunar and Planetary Science Conference* (pp. 111–159). New York: Pergamon Press.

Dymek, R. F. (1986). Characterization of the Apollo 15 feldspathic basalt suite. In *Workshop on the Geology and Petrology of the Apollo 15 Landing Site* (pp.

52–57). Houston, TX: Lunar and Planetary Institute.

Elphic, R. C., Lawrence, D. J., Feldman, W. C., Barraclough, B. L., Maurice, S., Binder, A. B., and Lucey, P. G. (1998). Lunar Fe and Ti abundances: comparison of lunar prospector and clementine data. *Science*, *281*(5382), 1493–1496. https://doi.org/10.1126/science.281.5382.1493

Elphic, R. C., Lawrence, D. J., Feldman, W. C., Barraclough, B. L., Maurice, S., Binder, A. B., and Lucey, P. G. (2000). Lunar rare earth element distribution and ramifications for FeO and TiO2: Lunar Prospector neutron spectrometer observations. *J. Geophys. Res.*, *105*(E8), 20333–20345. https://doi.org/10.1029/1999JE001176

Elphic, R. C., Lawrence, D. J., Feldman, W. C., Barraclough, B. L., Gasnault, O. M., Maurice, S., Lucey, P. G., Blewett, D. T., and Binder, A. B. (2002). Lunar Prospector neutron spectrometer constraints on TiO2. *J. Geophys. Res.*, *107*(E4), 8-1–8-9. https://doi.org/10.1029/2000JE001460

Feldman, W. C., Barraclough, B. L., Maurice, S., Elphic, R. C., Lawrence, D. J., Thomsen, D. R., and Binder, A. B. (1998). Major compositional units of the moon: lunar prospector thermal and fast neutrons. *Science*, *281*(5382), 1489–1493. https://doi.org/10.1126/science.281.5382.1489

Feldman, W. C., Gasnault, O., Maurice, S., Lawrence, D. J., Elphic, R. C., Lucey, P. G., and Binder, A. B. (2002). Global distribution of lunar composition: New results from Lunar Prospector. *J. Geophys. Res.*, *107*(E3), 5-1–5-14. https://doi.org/10.1029/2001JE001506

Freed, A. M., Johnson, B. C., Blair, D. M., Melosh, H. J., Neumann, G. A., Phillips, R. J., Solomon, S. C., Wieczorek, M. A., and Zuber, M. T. (2014). The formation of lunar mascon basins from impact to contemporary form. *J. Geophys. Res.*, *119*(11), 2378–2397. https://doi.org/10.1002/2014JE004657

Gasnault, O., Feldman, W. C., Maurice, S., Genetay, I., d'Uston, C., Prettyman, T. H., and Moore, K. R. (2001). Composition from fast neutrons: application to the moon. *Geophys. Res. Lett.*, *28*(19), 3797–3800. https://doi.org/10.1029/2001GL013072

Gurtner, M., Desorgher, L., Flückiger, E. O., and Moser, M. R. (2006). A Geant4 application to simulate the interaction of space radiation with the Mercurian environment. *Adv. Space Res.*, *37*(9), 1759–1763. https://doi.org/10.1016/j.asr.2004.12.015

Hasebe, N., Shibamura, E., Miyachi, T., Takashima, T., Kobayashi, M. N., Okudaira, O., Yamashita, N., Kobayashi, S., Karouji, Y., … Kim, K. J. (2009). First results of high performance Ge gamma-ray spectrometer onboard lunar orbiter SELENE (KAGUYA). *J. Phys. Soc. Jpn.*, *78*(Suppl. A), 18–25. https://doi.org/10.1143/JPSJS.78SA.18

Haskin, L. A. (1998). The Imbrium impact event and the thorium distribution at the lunar highlands surface. *J. Geophys. Res.*, *103*(E1), 1679–1689. https://doi.org/10.1029/97JE03035

Heiken, G. H., Vaniman, D. T., and French, B. M. (1991). *Lunar Sourcebook: A User's Guide to the Moon*. Cambridge University Press.

Jolliff, B. L., Gillis, J. J., Haskin, L. A., Korotev, R. L., and Wieczorek, M. A. (2000). Major lunar crustal terranes: Surface expressions and crust-mantle origins. *J. Geophys. Res.*, *105*(E2), 4197–4216. https://doi.org/10.1029/1999je001103

Knoll, G. F. (2000). *Radiation Detection and Measurement*. New York: Wiley.

Kobayashi, S., Karouji, Y., Morota, T., Takeda, H., Hasebe, N., Hareyama, M., Kobayashi, M., Shibamura, E., Yamashita, N., … Ishihara, Y. (2012). Lunar farside Th distributi on measured by Kaguya gamma-ray spectrometer. *Earth Planet. Sci. Lett.*, *337-338*, 10–16. https://doi.org/10.1016/j.epsl.2012.05.007

Korotev, R. L., Jolliff, B. L., Zeigler, R. A., Gillis, J. J., and Haskin, L. A. (2003). Feldspathic lunar meteorites and their implications for compositional remote sensing of the lunar surface and the composition of the lunar crust. *Geochim. Cosmochim. Acta*, *67*(24), 4895–4923. https://doi.org/10.1016/j.gca.2003.08.001

Lawrence, D. J., Feldman, W. C., Elphic, R. C., Little, R. C., Prettyman, T. H., Maurice, S., Lucey, P. G., and Binder, A. B. (2002). Iron abundances on the lunar surface as measured by the Lunar Prospector gamma-ray and neutron spectrometers. *J. Geophys. Res.*, *107*(E12), 13-11–13-26. https://doi.org/10.1029/2001JE001530

Li, C. L., Liu, J. J., Ren, X., Mou, L. L., Zou, Y. L., Zhang, H. B., Lü, C., Liu, J. Z., Zuo, W., … Ouyang, Z. Y. (2010). The global image of the Moon obtained by the Chang'E-1: Data processing and lunar cartography. *Sci. China Earth Sci.*, *53*(8), 1091–1102. https://doi.org/10.1007/s11430-010-4016-x

Ling, Z. C., Zhang, J., Liu, J. Z., Zhang, W. X., Zhang, G. L., Liu, B., Ren, X., Mu, L. J., Liu, J. J., and Li, C. L. (2011). Preliminary results of TiO2 mapping using Imaging Interferometer data from Chang'E-1. *Chin. Sci. Bull.*, *56*(20), 2082–2087. https://doi.org/10.1007/s11434-011-4550-8

Ma, T., Chang, J., Zhang, N., Cai, M. S., Gong, Y. Z., Tang, H. S., Zhang, R. J., Wang. N. S., Yu, M., … Liu, L. G. (2008). Gamma-ray detector on board lunar mission Chang'E-1. *Adv. Space Res.*, *42*(2), 347–349. https://doi.org/10.1016/j.asr.2007.04.042

McKay, G. A. (1986). Topic 2: Apollo 15 KREEP basalt. In *Workshop on the Geology and Petrology of the Apollo 15 Landing Site* (pp. 14–16). Houston, TX: Lunar and Planetary Institute.

Melosh, H. J., Freed, A. M., Johnson, B. C., Blair, D. M., Andrews-Hanna, J. C., Neumann, G. A., Phillips, R. J., Smith, D. E., Solomon, S. C., … Zuber, M. T. (2013). The origin of lunar mascon basins. *Science*, *340*(6140), 1552–1555. https://doi.org/10.1126/science.1235768

Miljković, K., Wieczorek, M. A., Collins, G. S., Solomon, S. C., Smith, D. E., Zuber, M. T. (2015). Excavation of the lunar mantle by basin-forming impact events on the Moon. *Earth Planet. Sci. Lett.*, *409*, 243–251. https://doi.org/10.1016/j.epsl.2014.10.041

Montesi, L. G. J. (2013). Solving the mascon mystery. *Science*, *340*(6140), 1535–1536. https://doi.org/10.1126/science.1238099

Norman, M. D., and Ryder, D. (1980). Geochemical constraints on the igneous evolution of the lunar crust. In *Proceedings of the 11th Lunar and Planetary Science Conference* (pp. 317–331). New York: Pergamon Press.

Ohishi, M., Mori, M., and Walker, W. (2004). Gamma-ray spectra due to cosmic-ray interactions with dense gas clouds. *Astrophys. J.*, *610*(2), 868–875. https://doi.org/10.1086/421732

Ouyang, Z. Y., Li, C. L., Zou, Y. L., Zhang, H. B., Lü, C., Liu, J. Z., Liu, J. J., Zuo, W., Su, Y., … Gao, G. N. (2011). Primary scientific results of Chang'E-1 lunar mission. *Sci. China Earth Sci.*, *53*(11), 1565–1581. https://doi.org/10.1007/s11430-010-4056-2

Phillips, R. J., and Lambeck, K. (1980). Gravity fields of the terrestrial planets: Long-wavelength anomalies and tectonics. *Rev. Geophys. Space Phys.*, *18*(1), 27–76. https://doi.org/10.1029/RG018i001p00027

Reedy, R. C. (1978). Planetary gamma-ray spectroscopy. In *Proceedings of the 9th Lunar Science Conference* (pp. 2961–2984). New York: Pergamon Press.

Reedy, R. C. (2000). Predicting the production rates of cosmogenic nuclides. *Nucl. Instrum. Methods Phys. Res. B*, *172*(1-4), 782–785. https://doi.org/10.1016/S0168-583X(00)00107-5

Reedy, R. C. (2013). Cosmogenic-nuclide production rates: reaction cross section update. *Nucl. Instrum. Methods Phys. Res. B*, *294*, 470–474. https://doi.org/10.1016/j.nimb.2011.08.034

Taylor, S. R. (1982). Planetary science: a lunar perspective. Houston: Lunar and Planetary Institute.

Taylor, S. R., Taylor, G. J., and Taylor, L. A. (2006). The moon: a Taylor perspective. *Geochim. Cosmochim. Acta*, *70*(24), 5904–5918. https://doi.org/10.1016/j.gca.2006.06.262

Taylor, S. R. (2014). The Moon re-examined. *Geochim. Cosmochim. Acta*, *141*, 670–676. https://doi.org/10.1016/j.gca.2014.06.031

Thorey, C., Michaut, C., and Wieczorek, M. (2015). Gravitational signatures of lunar floor-fractured craters. *Earth Planet. Sci. Lett.*, *424*, 269–279. https://doi.org/10.1016/j.epsl.2015.04.021

Warren, P. H. (1993). A concise compilation of petrologic information on possibly pristine nonmare Moon rocks. *Am. Mineral.*, *78*, 360–376.

Warren, P. H. (2005). "New" lunar meteorites: implications for composition of the global lunar surface, lunar crust, and the bulk Moon. *Meteorit. Planet. Sci.*, *40*(3), 477–506. https://doi.org/10.1111/j.1945-5100.2005.tb00395.x

Wise, D. U., and Yates, M. T. (1970). Mascons as structural relief on a lunar 'moho'. *J. Geophys. Res.*, *75*(2), 261–268. https://doi.org/10.1029/JB075i002p00261

Yamashita, N., Hasebe, N., Miyachi, T., Kobayashi, M., Okudaira, O., Kobayashi, S., Ishizaki, T., Sakurai, K., Miyajima, M., … Gasnault, O. (2008). Complexities of gamma-ray line intensities from the lunar surface. *Earth Planets Space*, *60*(4), 313–319. https://doi.org/10.1186/BF03352796

Yan, B. K., Xiong, S. Q., Wu, Y. Z., Wang, Z. C., Dong, L. N., Gan, F. P., Yang, S. M.,

and Wang, R. S. (2012). Mapping Lunar global chemical composition from Chang'E-1 IIM data. *Planet. Space Sci.*, *67*(1), 119–129. https://doi.org/10.1016/j.pss.2012.03.010

Yang, J., Ge, L. Q., Xiong, S. Q., Zhang, Q. X., and Gu, Y. (2013). Global distribution analysis of potassium on lunar surface using CE1-GRS data. *At. Energy Sci. Technol.*, *47*(8), 1417–1421. https://doi.org/10.7538/yzk.2013.47.08.1417

Zhang, Q. X., Ge, L. Q., Gu, Y., Lin, Y. C., Zeng, G. Q., and Yang, J. (2012). Background estimation based on Fourier Transform in the energy-dispersive X-ray fluorescence analysis. *X-Ray Spectrom.*, *41*(2), 75–79. https://doi.org/10.1002/xrs.2360

Zhu, M. H., Ma, T., and Chang, J. (2010). Chang'E-1 gamma ray spectrometer and preliminary radioactive results on the lunar surface. *Planet. Space Sci.*, *58*(12), 1547–1554. https://doi.org/10.1016/j.pss.2010.07.022

Zhu, M. H., Ma, T., Chang, J., Tang, Z. S., Ip, W. H., and Xu, A. A. (2011). Lunar potassium distribution: Results from Chang'E-1 gamma ray spectrometer. *Sci. China Phys. Mech. Astron.*, *54*(11), 2083–2090. https://doi.org/10.1007/s11433-011-4491-x

Zhu, M. H., Chang, J., Ma, T., Ip, W. H., Fa, W. Z., Wu, J., Cai, M. S., Gong, Y. Z., Hu, Y. M., … Tang, Z. S. (2013). Potassium map from Chang ' E-2 constraints the impact of crisium and orientale basin on the moon. *Sci. Rep.*, *3*, 1611. https://doi.org/10.1038/srep01611

Zhu, M. H., Chang, J., Xie, M. G., Fritz J., Fernandes, V. A., Ip, W. H., Ma, T., and Xu, A. (2015). The uniform K distribution of the mare deposits in the Orientale Basin: Insights from Chang'E-2 gamma-ray spectrometer. *Earth Planet. Sci. Lett.*, *418*, 172–180. https://doi.org/10.1016/j.epsl.2014.11.009